*Acta Oceanol. Sin.*, 2021, Vol. 40, No. 5, P. 94–104
https://doi.org/10.1007/s13131-021-1724-3
http://www.hyxb.org.cn
E-mail: ocean2@hyxb.org.cn

# Variations in melt supply along an orthogonal supersegment of the Southwest Indian Ridge (16°–25°E)

Caicai Zha[1, 2, 3, 5, 6], Jian Lin[1, 2, 3, 4, 6*], Zhiyuan Zhou[1, 2, 3], Xubo Zhang[1, 2, 3], Min Xu[1, 2, 3], Fan Zhang[1, 2, 3]

[1] Key Laboratory of Ocean and Marginal Sea Geology, South China Sea Institute of Oceanology, Innovation Academy of South China Sea Ecology and Environmental Engineering, Chinese Academy of Sciences, Guangzhou 510301, China

[2] Southern Marine Science and Engineering Guangdong Laboratory (Guangzhou), Guangzhou 511458, China

[3] China-Pakistan Joint Research Center on Earth Sciences, CAS-HEC, Islamabad 45320, Pakistan

[4] Department of Geology and Geophysics, Woods Hole Oceanographic Institution, Woods Hole, MA 02543, USA

[5] University of Chinese Academy of Sciences, Beijing 100049, China

[6] Department of Ocean Science and Engineering, Southern University of Science and Technology, Shenzhen 518055, China

Received 5 March 2020; accepted 3 May 2020



**Abstract**

The orthogonal supersegment of the ultraslow-spreading Southwest Indian Ridge at 16°–25°E is characterized by significant along-axis variations of mantle potential temperature. A detailed analysis of multibeam bathymetry, gravity, and magnetic data were performed to investigate its variations in magma supply and crustal accretion process. The results revealed distinct across-axis variations of magma supply. Specifically, the regionally averaged crustal thickness reduced systematically from around 7 Ma to the present, indicating a regionally decreasing magma supply. The crustal structure is asymmetric in regional scale between the conjugate ridge flanks, with the faster-spreading southern flank showing thinner crust and greater degree of tectonic extension. Geodynamic models of mantle melting suggested that the observed variations in axial crustal thickness and major element geochemistry can be adequately explained by an eastward decrease in mantle potential temperature of about 40°C beneath the ridge axis. In this work, a synthesized model was proposed to explain the axial variations of magma supply and ridge segmentation stabilities. The existence of large ridge-axis offsets may play important roles in controlling melt supply. Several large ridge-axis offsets in the eastern section (21°–25°E) caused sustained along-axis focusing of magma supply at the centers of eastern ridge segments, enabling quasi-stable segmentation. In contrast, the western section (16°–21°E), which lacks large ridge-axis offsets, is associated with unstable segmentation patterns.

**Key words:** ultraslow-spreading ridge, Southwest Indian Ridge, ridge segmentation, asymmetric accretion, melt supply, mantle temperature gradient

**Citation:** Zha Caicai, Lin Jian, Zhou Zhiyuan, Zhang Xubo, Xu Min, Zhang Fan. 2021. Variations in melt supply along an orthogonal supersegment of the Southwest Indian Ridge (16°–25°E). Acta Oceanologica Sinica, 40(5): 94–104, doi: 10.1007/s13131-021-1724-3

## 1 Introduction

The segmentation of mid-ocean ridges has long been recognized as a fundamental feature of the seafloor spreading system, and different orders of ridge-axis discontinuities have been classified (Schouten et al., 1985; Macdonald et al., 1991). The first-order transform faults (TFs) offset the ridge-axis by strike-slip faults, typically with offset length of more than 30 km (e.g., Macdonald et al., 1991; Fox and Gallo, 1984). The second-order non-transform discontinuities (NTDs) typically have smaller offsets (about 2–30 km) (e.g., Macdonald et al., 1991; Sempéré et al., 1993). From the perspective of magmatic segmentation, segment centers are fed by focused magma supply and are thus associated with shallower seafloor and thicker crust, while the NTDs at the segment ends have less magma supply and deeper ridge-axis valleys (Lin et al., 1990; Tolstoy et al., 1993; Canales et al., 2000; Hooft et al., 2000; Hosford et al., 2001; Carbotte et al., 2015). Segments fed by more robust magma supply could migrate along the ridge axis, forming V-shaped NTD traces on both flanks (e.g., Gente et al., 1995; Tucholke et al., 1997; Wang et al., 2015; Dannowski et al., 2018; Zheng et al., 2019).

Many of the NTDs show long-lived characteristics, leaving clear tracks on ridge flanks that could be traced as coherent zones for millions of years (Pariso et al., 1995; Tucholke et al., 1997; Wang et al., 2015; Zheng et al., 2019). In contrast, some oth-

Foundation item: The Program of Southern Marine Science and Engineering Guangdong Laboratory (Guangzhou) under contract No. GML2019ZD0205; the National Natural Science Foundation of China under contract Nos 41890813, 41976066, 41976064, 91858207, 91958211 and 91628301; the Program of Chinese Academy of Sciences under contract Nos Y4SL021001, QYZDY-SSW-DQC005 and 133244KYSB20180029; the National Key Research and Development Program of China under contract Nos 2018YFC0309800 and 2018YFC0310105; the Guangdong Basic and Applied Basic Research Foundation under contract No. 2021A1515012227; the Program of China Ocean Mineral Resources Research and Development Association under contract No. DY135-S2-1-04.
*Corresponding author, E-mail: jlin@whoi.edu

er NTDs are relatively short-lived, experiencing rapid migration and emergence/demise in short episodes, resulting in irregular-shaped configurations on ridge flanks (e.g., Gente et al., 1995; Cannat et al., 2003). Although NTDs are widely observed at slow- and ultraslow-spreading ridges, the tectonic factors controlling their stability are still poorly understood.

The Southwest Indian Ridge (SWIR) is the longest ultraslow-spreading (14–16 mm/a, Patriat et al., 1997) ridge system on earth. The SWIR exhibits strong along-axis variations in ridge-axis morphology and crustal structure (Grindlay et al., 1998; Georgen et al., 2001; Sauter et al., 2001; Cannat et al., 2003; Dick et al., 2003), providing a unique opportunity to investigate ridge segment evolution and stability at an ultraslow-spreading rate. The ridge segments within the orthogonal supersegment of the SWIR at 16°–25°E show distinct variations in segment stability and off-axis structure (Fig. 1). The off-axis TF/NTD traces are coherent in the eastern section (21°–25°E) near the Du Toit and Andrew Bain TFs and can be traced out to at least 60 Ma. The S-shaped curvatures of the TF/NTD are visible on the residual free-air gravity anomaly (RFAA, the calculating method is shown in Fig. S1) map, revealing a complex history of rapid plate motion changes of the SWIR (Bernard et al., 2005). In contrast, the western section (16°–21°E) lacks coherent off-axis NTD traces (Fig. 1).

Previous studies have revealed significant spatial variations in geophysical anomalies and geochemical characteristics along this orthogonal supersegment. Grindlay et al. (1998) suggested that the western and eastern sections of the orthogonal supersegment were underlain by relatively warm and cold mantle, re-

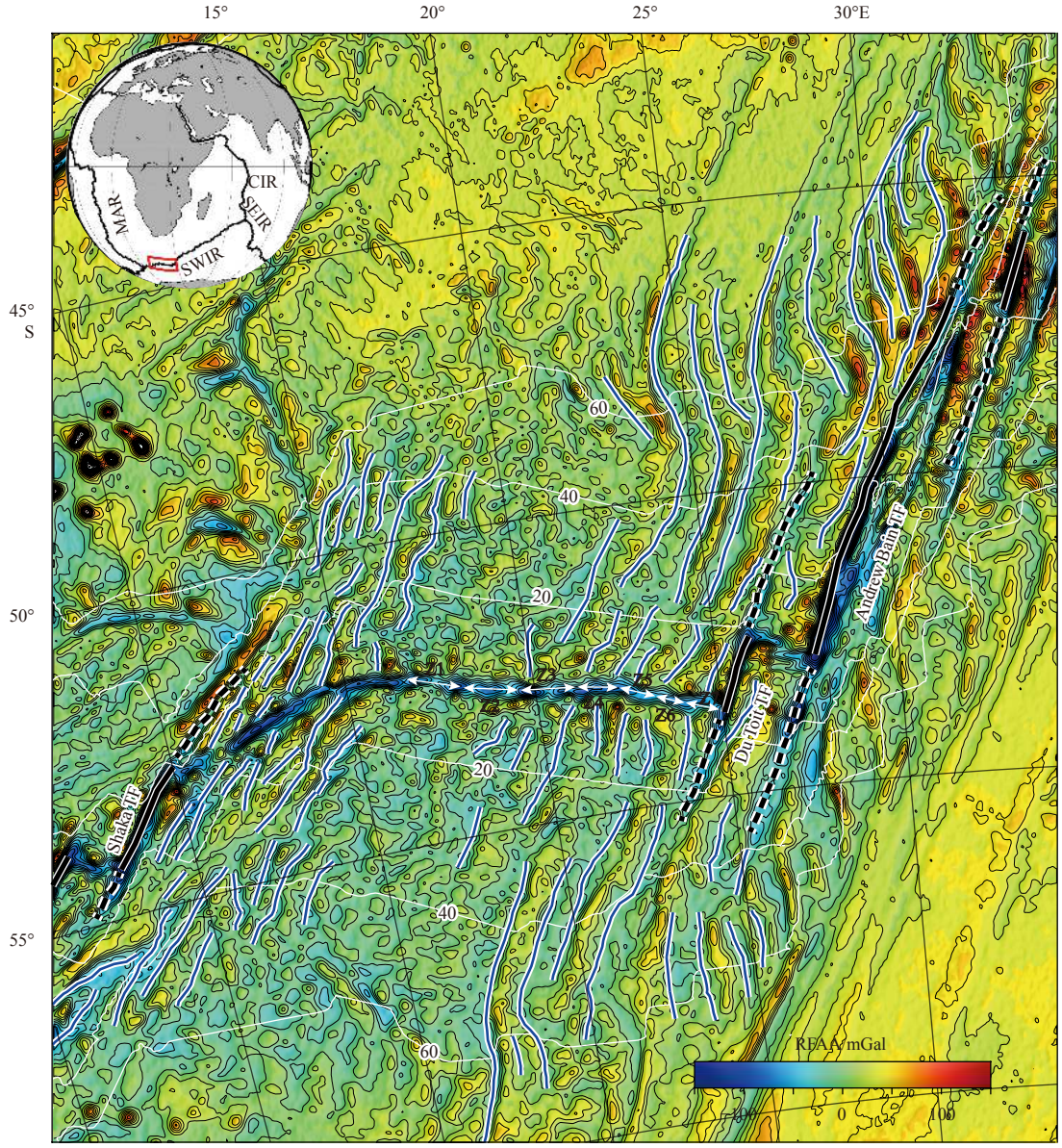


**Fig. 1.** Residual free-air gravity anomaly (RFAA) of the Southwest Indian Ridge at 4°–35°E. The RFAA is calculated from the latest global marine gravity model (Sandwell et al., 2014) after subtracting the crustal age-dependent component (Fig. S1). Segment boundaries are marked by thick black (transform faults and fracture zones) and blue (non-transform discontinuities) lines, respectively. Thin white lines mark crustal age isochrones from Müller et al. (2008). White double arrows show the location of axial zones as defined in Fig. 2. Shaka TF: Shaka transform fault; Du Toit TF: Du Toit transform fault; Andrew Bain TF: Andrew Bain transform fault. The red box in the inset shows the location of the study area. CIR: Central Indian Ridge; SEIR: Southeast Indian Ridge; SWIR: Southwest Indian Ridge; MAR: Mid-Atlantic Ridge.

spectively. Standish et al. (2008) analyzed basalt samples collected along the orthogonal supersegment (Dick et al., 2003), revealing eastward decreases in the average mantle melting degree (based on $Na_{8.0}$) and initial mantle melting depth (based on $Fe_{8.0}$), which is consistent with the overall eastward decrease in crustal thickness. The combined geological, geophysical, and geochemical data thus offer an excellent opportunity to investigate ridge segmentation, crustal structure, and mantle melting at an ultraslow-spreading ridge.

In this study, the spatial and temporal variations of crustal production along the SWIR at 16°–25°E were investigated by analyzing on- and off-axis multibeam bathymetry, shipboard gravity, and magnetic data. The along-axis variations in mantle potential temperature and melting were estimated by using the observed major element geochemistry and gravity-derived crustal thickness and geodynamic models of mantle melting. Finally, a synthesized geological model was proposed to explain the differences in crustal production and segment stability between the western and eastern sections.

## 2 Data and methods

### 2.1 *Bathymetry*

Multibeam bathymetry data of the SWIR at 16°–25°E were collected during the KN145L16 Cruise in 1996 (Grindlay et al., 1998) and were downloaded from http://www.marine-geo.org. The multibeam data have a spatial resolution of about 100 m. For areas lacking multibeam coverage (e.g., the gaps between track lines and regions outside the survey area), the synthesized bathymetry from the combination of satellite gravity-derived bathymetry and shipboard measurements was used. The synthesized bathymetry has an average spatial resolution of 15 arc-seconds (Tozer et al., 2019), although the local resolution is variable (Zhang et al., 2019). A total of 12 ridge segments were identified based on ridge axis morphology and were given segment names of S3–S14 based on the definition of Grindlay et al. (1998) (Fig. 2).

### 2.2 *Magnetics*

The magnetic data were obtained from the database of DeMets et al. (2015), including data collected by research cruises of multiple countries. DeMets et al. (2015) identified magnetic anomalies in nearly 7 000 shiptrack lines and selected 4 822 reversal crossings to construct a relatively high-resolution crustal age model of the SWIR from about 20 Ma to the present. The estimated average spreading rates on the southern and northern flanks were 0.74 cm/a and 0.6 cm/a, respectively (Fig. S2).

### 2.3 *Mantle Bouguer anomaly*

To obtain the mantle Bouguer anomaly (MBA) (Fig. 3a), the gravitational effects of the water/upper crust, upper/lower crust, and lower crust/mantle interfaces were subtracted from the free-air gravity anomaly (FAA), using the Fast Fourier Transform method of Parker (1973) and assuming a reference model with a 2-km-thick upper crust and a 4-km-thick lower crust (Grindlay et al., 1998). The densities of the seawater, upper crust, lower crust, and mantle were assumed to be 1 030 kg/m$^3$, 2 400 kg/m$^3$, 2 700 kg/m$^3$ and 3 300 kg/m$^3$, respectively.

### 2.4 *Thermal correction*

The regional thermal structure of a 100-km-thick mantle layer beneath an orthogonal ridge-transform-ridge system with an idealized surface plate geometry was calculated (Fig. S3). The actual plate boundary geometry was approximated using a series of ridge segments that are connected by orthogonal offsets. A 3D mantle velocity field assuming passive upwelling and the corresponding mantle temperature field were then calculated by using the methods of Phipps Morgan and Forsyth (1988) (Table 1). The asymmetric half-spreading rates, as described in Section 2.2 (Fig. S2), were imposed on the surface boundary. The calculated mantle temperature field was then converted to a 3D density grid, yielding the gravity effects of a mantle thermal structure (Georgen et al., 2001) (Fig. S3).

### 2.5 *Residual mantle Bouguer anomaly and crustal thickness*

Residual mantle Bouguer anomaly (RMBA) was obtained by subtracting the thermal corrections from the MBA. The resultant RMBA reflects spatial variations in crustal thickness and deviations from the assumed reference models of constant crustal and mantle densities (Fig. 3b).

An end-member model of crustal thickness variations was calculated by the downward continuation of the RMBA to a reference depth of 9 km below sea-level (i.e., the summation of the average crustal thickness of 6 km and average water depth of 3 km in the study area) (Fig. 3c). A crust/mantle density contrast of

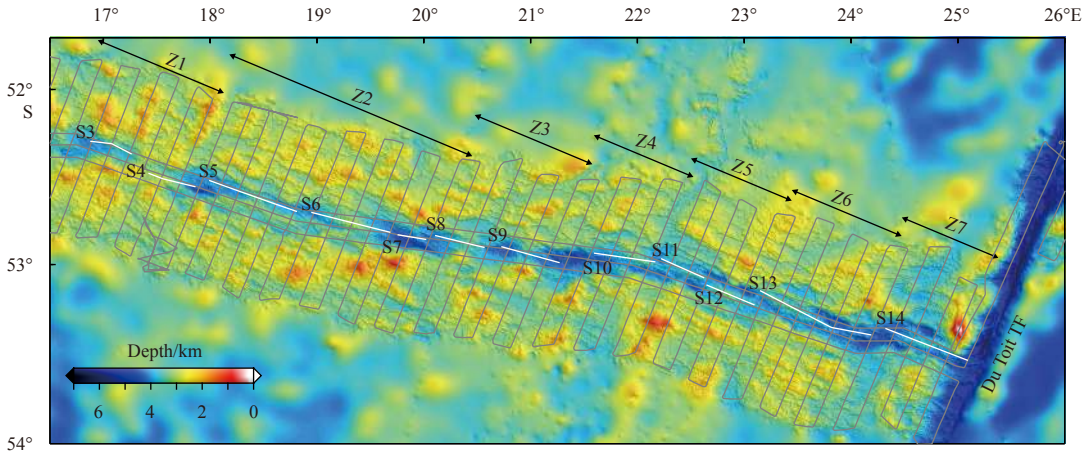


**Fig. 2.** Shaded-relief bathymetric map of the orthogonal supersegment, with multibeam bathymetry near the axis and satellite-derived bathymetry filling the gaps. The white lines indicate ridge segments. Segment names S3 to S14 are adopted from the definition of Grindlay et al. (1998). Z1 to Z7 are zones marked to facilitate analysis. Thin gray lines show the ship tracklines.

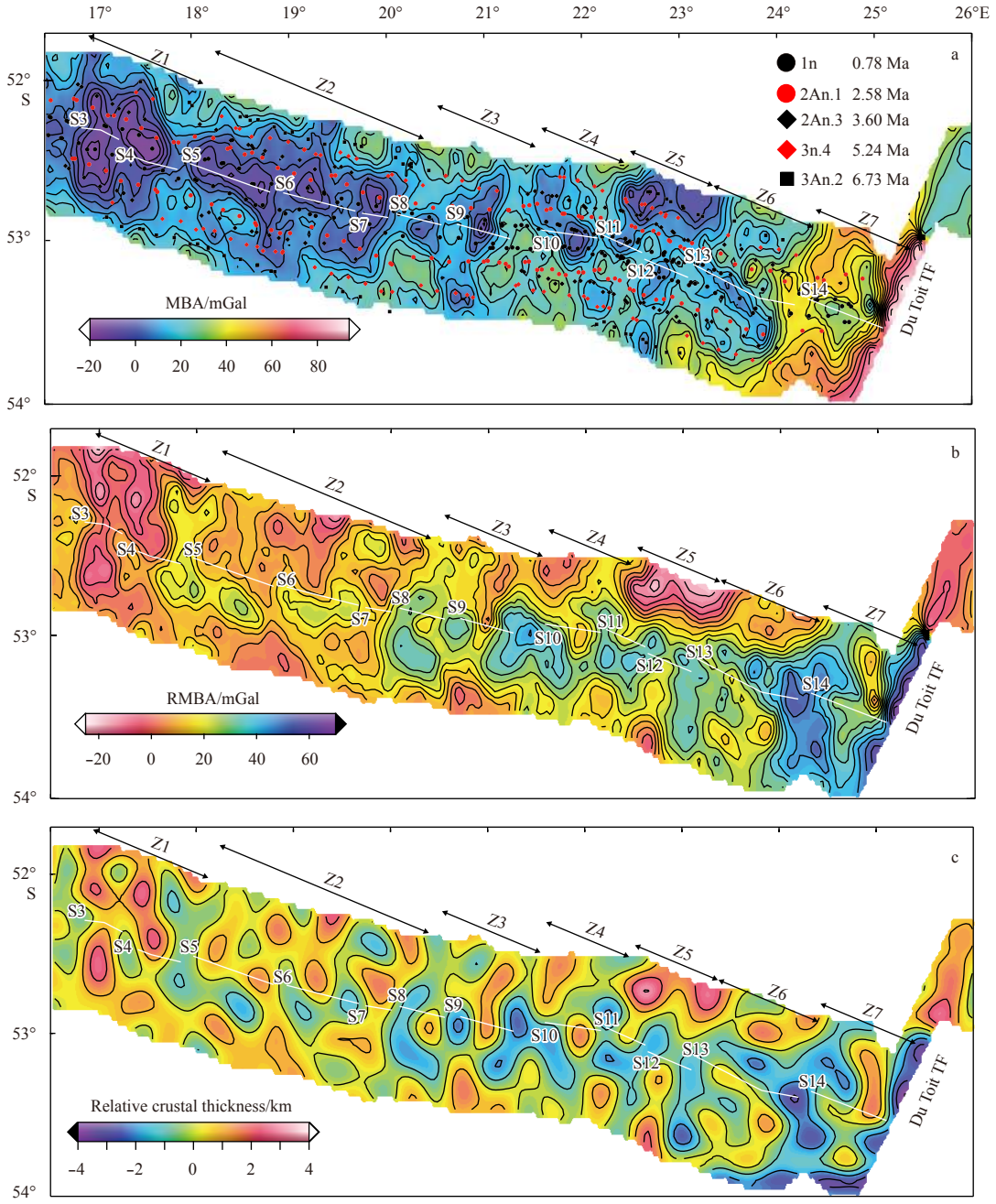


**Fig. 3.** Maps of mantle Bouguer anomaly (MBA) of the 16.5°–26°E area (a) (after Grindlay et al., 1998), the residual mantle Bouguer anomaly (RMBA) based on the thermal correction of Fig. S3 (b), and the relative crustal thickness derived from the downward continuation of the RMBA to a reference depth of 9 km (c). Labels are the same as in Fig. 2. The red and black dots in a are magnetic anomaly reversals from DeMets et al. (2015).

$0.6\times10^3$ kg/m$^3$ (e.g., Kuo and Forsyth, 1988; Lin et al., 1990) was assumed. To avoid instabilities that are inherent in the downward continuation of short-wavelength anomalies, a cosine taper filter was used to minimize the RMBA signals outside of the interested wavelength window between 25 km and 35 km.

### 2.6 *Modeling mantle melting, crustal thickness, and major element geochemistry*

Constrained by the observed variations of crustal thickness and major element geochemistry ($Na_{8.0}$ and $Fe_{8.0}$), a series of 2D mid-ocean ridge spreading models were constructed to estimate the mantle temperature gradient along the orthogonal superseg-ment (Gregg et al., 2009; Zhang et al., 2018). In the 2D numerical models, the top surface plates were assumed to move apart at a mean half-spreading rate $U$=0.67 cm/a, and the surface mantle temperature was fixed at $T_0$=0°C; meanwhile, the base of the model domain at depth $D$=100 km was set as an open boundary with a given mantle potential temperature $T_p$. The sides of the model domain were set as open boundaries with no horizontal heat flux. The full model parameters were given in Table 2. Based on the calculated mantle flow and thermal structure, the BG15 melting model with a constant melt productivity of 0.1 GPa$^{-1}$ (Behn and Grove, 2015) was used to estimate melt fraction and resultant melt composition at each grid in the model domain.

**Table 1.** Parameters used in modeling 3D mantle temperature field

| Parameter | Description | Value |
|---|---|---|
| $\rho_m$/(kg·m$^{-3}$) | mantle density | 3 300 |
| $C_p$/(J·kg$^{-1}$·K$^{-1}$) | specific heat capacity | 1 250 |
| $\kappa$/(W·m$^{-1}$·K$^{-1}$) | thermal conductivity | 3 |
| $Q$/(J·mol$^{-1}$) | activation energy | 2.5×10$^5$ |
| $R$/(J·mol$^{-1}$·K$^{-1}$) | universal gas constant | 8.311 4 |
| $T_s$/°C | surface temperature | 0 |
| $T_p$/°C | mantle potential temperature | 1 350 |
| $U_n$/(mm·a$^{-1}$) | half–spreading rate in northern flank | 6.0 |
| $U_s$/(mm·a$^{-1}$) | half–spreading rate in southern flank | 7.4 |
| $g$/(m·s$^{-2}$) | gravitational acceleration | 9.8 |

**Table 2.** Parameters used in modeling 2D mantle melting field

| Parameter | Description | Value |
|---|---|---|
| $\rho$/(kg·m$^{-3}$) | mantle density | 3 300 |
| $\eta_0$/(Pa·s) | reference viscosity | 10$^{19}$ |
| $\eta_{max}$/(Pa·s) | maximum viscosity | 10$^{23}$ |
| $C_p$/(J·kg$^{-1}$·K$^{-1}$) | specific heat capacity | 1 250 |
| $k$/(W·m$^{-1}$·K$^{-1}$) | thermal conductivity | 3 |
| $Q$/(J·mol$^{-1}$) | activation energy | 2.5×10$^5$ |
| $R$/(J·mol$^{-1}$·K$^{-1}$) | universal gas constant | 8.311 4 |
| $T_s$/°C | temperature at the surface of the thermal model | 0 |
| $T_p$/°C | mantle potential temperature | 1 320–1 400 |
| $U$/(mm·a$^{-1}$) | half spreading rate | 6.7 |
| $g$/(m·s$^{-2}$) | gravitational acceleration | 9.8 |

The crustal thickness at the ridge axis was calculated by integrating the melt production rate over the melting region divided by the spreading rate (Forsyth, 1993). This model assumed that the melt first migrated vertically, then moved laterally along a low permeability boundary (e.g., bottom of the mantle lithosphere), and finally aggregated beneath the ridge axis (e.g., Sparks et al., 1993; Magde and Sparks, 1997). The major element compositions of the melt aggregated beneath the ridge axis were estimated by pooling all incremental melt compositions and weighing them by the melt production rate (Behn and Grove, 2015). The melt production rate was defined as the product of the melt productivity and mantle upwelling velocity. In addition, to compare with the observed $Na_{8.0}$ and $Fe_{8.0}$, the model of Yang et al. (1996) was used to calculate the fractional crystallization path of the aggregated melt. The pressure of crystallization was assumed to be 0.1 GPa (Standish et al., 2008).

## 3 Results

### 3.1 *Along-axis variations in morphology and MBA*

The along-axis topography west of 21.5°E (segments S3 to S9) shows a regional eastward decreasing trend, and local variations within segments S10 to S13 appear to be superimposed on the regional topographic trend. Segment S14 is directly affected by the thermal effect of the 150-km-long Du Toit transform fault (DTTF) (red line in Fig. 4a). The along-axis variations in MBA, with an amplitude of up to 90 mGal, reveal a regional eastward increasing trend from a local minimum at 17.5°E (–20 mGal) to a maximum (70 mGal) at the eastern ridge-transform intersection (RTI). The calculated along-axis thermal effect of the DTTF is about 37 mGal and is limited to a region east of 23.2°E within a distance of about 125 km west of the RTI (Fig. 4b). Thus, the abrupt increases in the

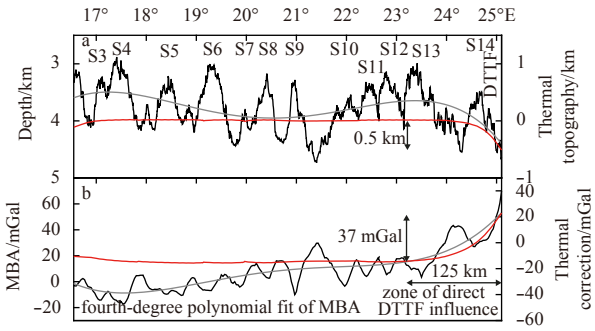


**Fig. 4.** Axial variations of observed and calculated depth and gravity anomalies. a. Along-axis variations of topography (black line) and thermal isostatic topography (red line). Labels in the upper panel show the segments named by Grindlay et al. (1998) as in Fig. 2. DTTF: Du Toit transform fault. b. Along-axis variations of MBA (black line) and the calculated gravity effect of 3D plate cooling (red line). The thick gray line is the fourth-degree polynomial fit of the mantle Bouguer anomaly (MBA).

MBA east of 23.2°E could be explained by the DTTF thermal cooling effect, as predicted by the 3D passive mantle upwelling model. However, the remaining regional eastward increase of the MBA west of 23.2°E can not be explained by the DTTF cooling effect (Fig. 4b).

### 3.2 *Zones of distinct characteristics in morphology and MBA*

The results show that the off-axis morphology of the orthogonal supersegment varies strongly along ridge strike, with some segments have relatively coherent off-axis NTD traces while others do not (Figs 1 and 2). To better illustrate the differences between areas with relatively stable versus unstable segmentation, the study area was divided into seven zones (Z1–Z7, Figs 2 and 3) according to the characteristic variation patterns of the morphology and MBA.

The western-most zone Z1 is characterized by uplifted topography, small abyssal hills, and numerous volcanic cones. Linear abyssal hills are pervasive in the western part of zone Z2, while the eastern part is characterized by V-shaped topographic highs on both flanks. zones Z3 and Z4 are in a discordant zone, and the overall strike of the axial valley is approximately 10° counterclockwise from the regional strike of the orthogonal supersegment (Grindlay et al., 1998). The ridge axis has a relatively large offset that is associated with a wide and deep inter-segment basin between segments S9 and S10. The off-axis morphology in zones Z3 and Z4 are dominated by blocky terrains. Further east, zone Z5 has two well-defined ridge segments (segments S11 and S12 in Fig. 2), the V-shaped NTD traces on the ridge flanks indicate westward migration of segment S13 in zone Z6. Segment S14 in zone Z7 appears to have formed just a few million years ago in association with the westward migration of segment S13 (Figs 1 and 2).

The MBA, RMBA and relative crustal thickness show strong along- and across-axis variations (Fig. 3). Zone Z1 contains a large domain of negative MBA, and the thicker crust within zone Z1 indicates that this is an area of relatively robust magma supply. The MBA in zone Z2 is well elongated along the ridge axis with the most negative values slightly shift to the northern flank. The RMBA in zone Z2 varies little on the northern flank, but has three prominent positive domains on the southern flank. Zone Z3 is characterized by two small circular MBA lows that correspond to the two axial neovolcanic zones. Zone Z4 is characterized by a

strongly asymmetric MBA pattern between conjugate ridge flanks, with the southern flank showing more positive MBA. Zone Z5 has a domain of large negative MBA on the northern flank. Crustal thickness appears to have decreased from the ridge flanks to the spreading axis. Zone Z6 shows strong variations in the MBA across the ridge axis, with alternating thicker and thinner crust on both flanks. Lastly, zone Z7 is adjacent to the DTTF and shows the most positive MBA among all zones. A domain of relatively thick crust is located at the inside corner, coinciding with a large seamount (Grindlay et al., 1998).

### 3.3 *Across-axis variations in MBA, RMBA, and crustal thickness*

The MBA contains effects of long-wavelength plate cooling and short-wavelength crustal thickness fluctuations in across-axis direction. The observed across-axis variations in the MBA for some zones (e.g., zones Z1 and Z2) appear to fit well with the long-wavelength predictions of the 3D plate cooling model. Meanwhile, other zones show relatively large deviations either on both flanks (e.g., zones Z3, Z4, and Z5) or only on the northern flank (e.g., zones Z6 and Z7; Fig. 5).

The regionally averaged RMBA shows a general trend of increase from the ridge flanks to the spreading axis, while there is considerable local variability in the near axis part on the southern flank (Fig. 6). Furthermore, the regionally averaged RMBA shows significant asymmetry between the conjugate flanks, with relatively more positive RMBA on the southern flank (Fig. 6). However, the locally averaged RMBA and crustal thickness show large variations both along- and across-axis directions in each zone (Fig. 7). Zones Z1 and Z2 have thicker crust and their calculated across-axis fluctuations are less than 1 km (Fig. 7c). In contrast, the crustal thickness variations in the further eastern zones (zones Z3 to Z7) are larger and more complicated (Figs 7a and b). Zone Z5 has crustal thickness fluctuations of up to 2.5 km, which is the largest variation among all zones (Fig. 7c). The thickest part of zone Z5 is in the distal northern flank (Fig. 7b). The across-axis crustal thickness variations in zones Z3 and Z4 are about 1.5 km, while in zones Z6 and Z7, the variations are more than 2 km (Fig. 7c).

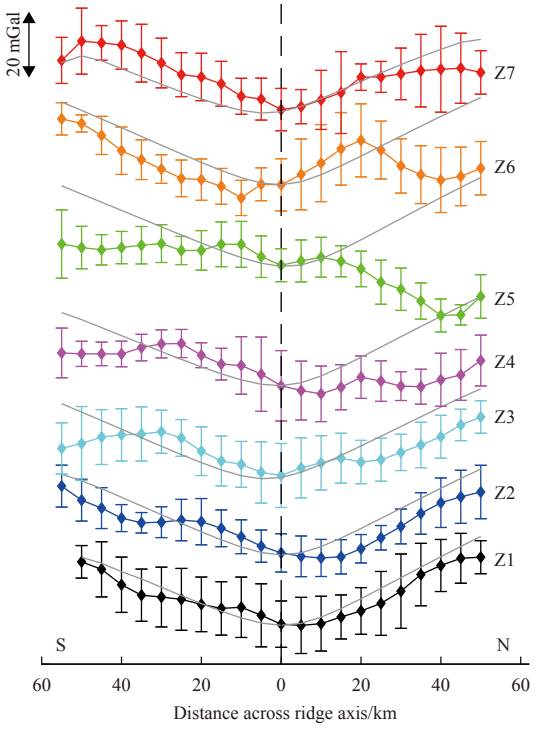


**Fig. 5.** Averaged across-axis variations in MBA along ship tracks in each zone. Gray lines are the averaged values of the calculated gravity effect due to 3D thermal cooling from Fig. 2c; the baseline value of the thermal cooling effect for the entire study area was shifted to match the observed overall values of the axial MBA profiles. The dashed black line indicates the ridge axis position. For illustration purpose, the baselines of each profile pair are shifted. S: south; N: north.

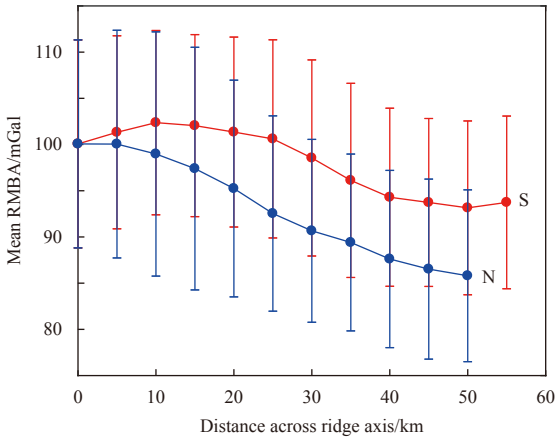


**Fig. 6.** Regionally averaged across-axis variations of RMBA at conjugate ridge flanks in all zones. S: south; N: north.

### 3.4 *Mantle temperature variations based on geochemical and geophysical constraints*

The along-axis residual topography and RMBA show correlated variations, with shallow topography and negative RMBA at segment centers (Figs 8a and b). The NTDs between segments S9 and S10 and between S13 and S14 are associated with deeper topography and more positive RMBA than that of DTTF (Figs 8a and b). These NTDs make segments S9, S10, S13, and S14 possess the prominent intra-segment RMBA variations (Fig. 8c). The observed geochemical variations ($Na_{8.0}$ and $Fe_{8.0}$) along the orthogonal supersegment are best-fitted by models with mantle potential temperate of 1 340–1 380°C. The estimated mantle potential temperature is approximately 1 380°C at the western end of the study region and approximately 1 340°C at the eastern end (Figs 8e and f). The mantle melting models predict a change of about 2 km in crustal thickness for a mantle potential temperature change of 40°C, and this result is consistent with the observed gradual westward increase in the gravity-derived crustal thickness (Fig. 8d).

In addition, the intra-segment mean variations and limits of the along-axis in $Na_{8.0}$, $Fe_{8.0}$ and RMBA were calculated. The segment-averaged $Na_{8.0}$ shows negative and positive correlations with the segment-averaged $Fe_{8.0}$ (Fig. 9a) and RMBA (Fig. 9b), respectively. Meanwhile, the segment-averaged $Fe_{8.0}$ shows negative correlation with the RMBA (Fig. 9c). The western most part, which has a mantle potential temperature of 1 380°C, is associated with deeper initial mantle melting depth, higher maximum mantle melting degree, and larger size of melting zone (Fig. 9d).

## 4 Discussion

### 4.1 *Implications of across-axis variations in RMBA*

The temporal changes in magma supply of a ridge segment can be reflected in across-axis variations in RMBA (e.g., Pariso et

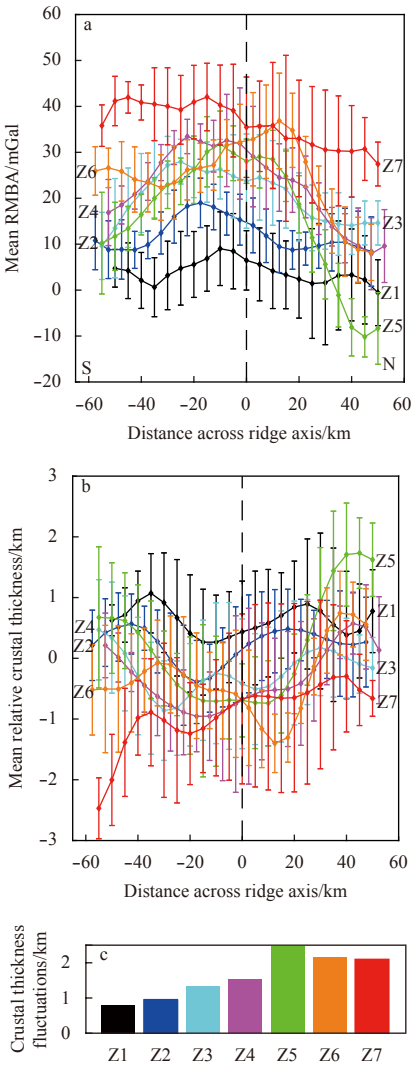


**Fig. 7.** Averaged across-axis variations of RMBA (a) and relative crustal thickness (b) for each zone, and fluctuations of averaged across-axis crustal thickness variations for each zone (c). The dashed black lines in panels a and b indicate the ridge axis position. S: south; N: north.

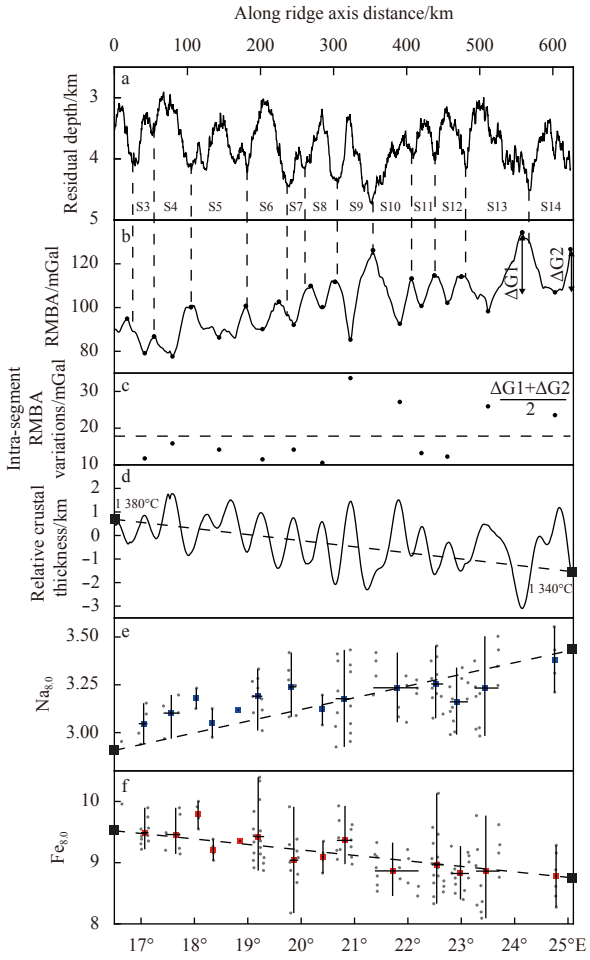


**Fig. 8.** Along-axis variations of residual topography (a), RMBA (b), average intra-segment RMBA variations (c), relative crustal thickness (d) $Na_{8.0}$ (e), and $Fe_{8.0}$ (f). The original data of $Na_{8.0}$ and $Fe_{8.0}$ (gray dots) are from Standish et al. (2008). In a, S3–S14 mark the segment numbers. Vertically dashed lines indicate the segment ends. Vertical arrows in b indicate the intra-segment RMBA variations (ΔG1, ΔG2). The formula for calculating the averaged intra-segment RMBA variations is given at the upper right of c. Horizontal dashed line in c show the mean variations of intra-segment RMBA variations. Horizontal and vertical thin black lines in e and f show the along-axis extent and the limits of each bin in averaging the $Na_{8.0}$ and $Fe_{8.0}$ values, and blue and red squares show the average intra-segment $Na_{8.0}$ and $Fe_{8.0}$ variations. Black dashed lines in d, e and f are the predicted changes from the melting models with mantle potential temperature of 1 340 °C at the eastern end and 1 380 °C at the western end as labeled in d.

al., 1995; Cannat et al., 2003; Wang et al., 2015; Zheng et al., 2019). The observed RMBA at the orthogonal supersegment shows strong across-axis variations. The regionally averaged RMBA show systematic increase from the ridge flanks to the axis (Fig. 6), indicating a regionally gradual reduction in magma from approximately 7 Ma to the present. The age-dependent fluctuations in the inferred magma supply are greater at the eastern section (zones Z5 to Z7) than that in the western section (zones Z1 to Z2) (Fig. 7c).

Furthermore, the southern flank appears to have thinner crust as indicated by the more positive RMBA on the regional scale (Fig. 6). The calculated average spreading rate of the southern flank is about 1.4 mm/a (i.e., around 21% of the average half-spreading rate) faster than that of the northern flank for the past 7 Ma (Fig. S2), suggesting that a greater amount of tectonic stretching might have occurred in the southern flank to accommodate faster spreading, which is similar to the local asymmetric spreading and tectonic extension of individual segments at the Mid-Atlantic Ridge (e.g., Escartín et al., 1999; Wang et al., 2015).

However, a single segment may have experienced a complex history of magmatic-tectonic variations, such as in segment S13 (Figs 3b and c). Together, the presented results reveal considerable spatial and temporal variations in the magmatic and tectonic processes of the ultraslow-spreading ridge.

### 4.2 *Contrasts between the western and eastern sections*

The western section (16°–21°E) of the orthogonal supersegment differs significantly from the eastern section (21°–25°E) in several important aspects: (1) ridge segments in the western section are relatively short lived (i.e., lack coherent off-axis NTD

traces, Grindlay et al., 1998) and are thus related to unstable segmentation. Some NTDs of the eastern section can be traced off-axis for tens of millions years (Figs 1 and 2) (Bernard et al., 2005) and are thus attributed to quasi-stable segmentation; (2) the ridge axis of the western section is associated with thicker crust, higher mantle melting degree (lower $Na_{8.0}$), and greater initial mantle melting depth of (higher $Fe_{8.0}$) than that of the eastern section (Figs 8d–f) (Standish et al., 2008). The best-fitting models show that the initial mantle melting depth is 72 km and that the maximum mantle melting degree can be up to 16% at the western most part, while those of the eastern most part are 60 km and 12%, respectively (Fig. 9d); (3) the inferred axial mantle potential temperature shows an eastward decrease of about 40°C along the orthogonal supersegment (Fig. 8), and this result is consistent with the estimation by a global joint inversion of ridge depth, major element geochemistry, and seismic shear wave velocity (Dalton et al., 2014); (4) the amplitude of the segment-scale along-axis variations in RMBA is the greatest at segments S9, S10, S13, and S14 (Fig. 8c); and this was interpreted to reflect the relatively strong along-axis focusing of melts (e.g., Lin and Phipps Morgan, 1992; Sauter et al., 2001; Cannat et al., 2003).

### 4.3 *A synthesized model of mantle melting and crustal structure*

A synthesized model of mantle melting and crustal structure of the orthogonal supersegment was proposed based on the combined constraints from the geophysical and geochemical data and geodynamical modeling (Fig. 10). In the synthesized model, the average mantle potential temperature is greater beneath the western section than that beneath the eastern section. The lowest mantle temperature is beneath segment S14, potentially reflecting the 3D mantle cooling effect of the DTTF (Fig. 4). Meanwhile, the amplitude of the segment-scale variations in crustal thickness (grey area, Fig. 10) may reflect melt focusing toward the centers of individual segments. Such melt focusing is the strongest at segments S9, S10, S13, and S14 (solid red arrows, Fig. 10), and is weaker at other segments, e.g., segments S5 and S6 (dashed red arrows, Fig. 10).

The off-axis stability of the ridge segments in the orthogonal

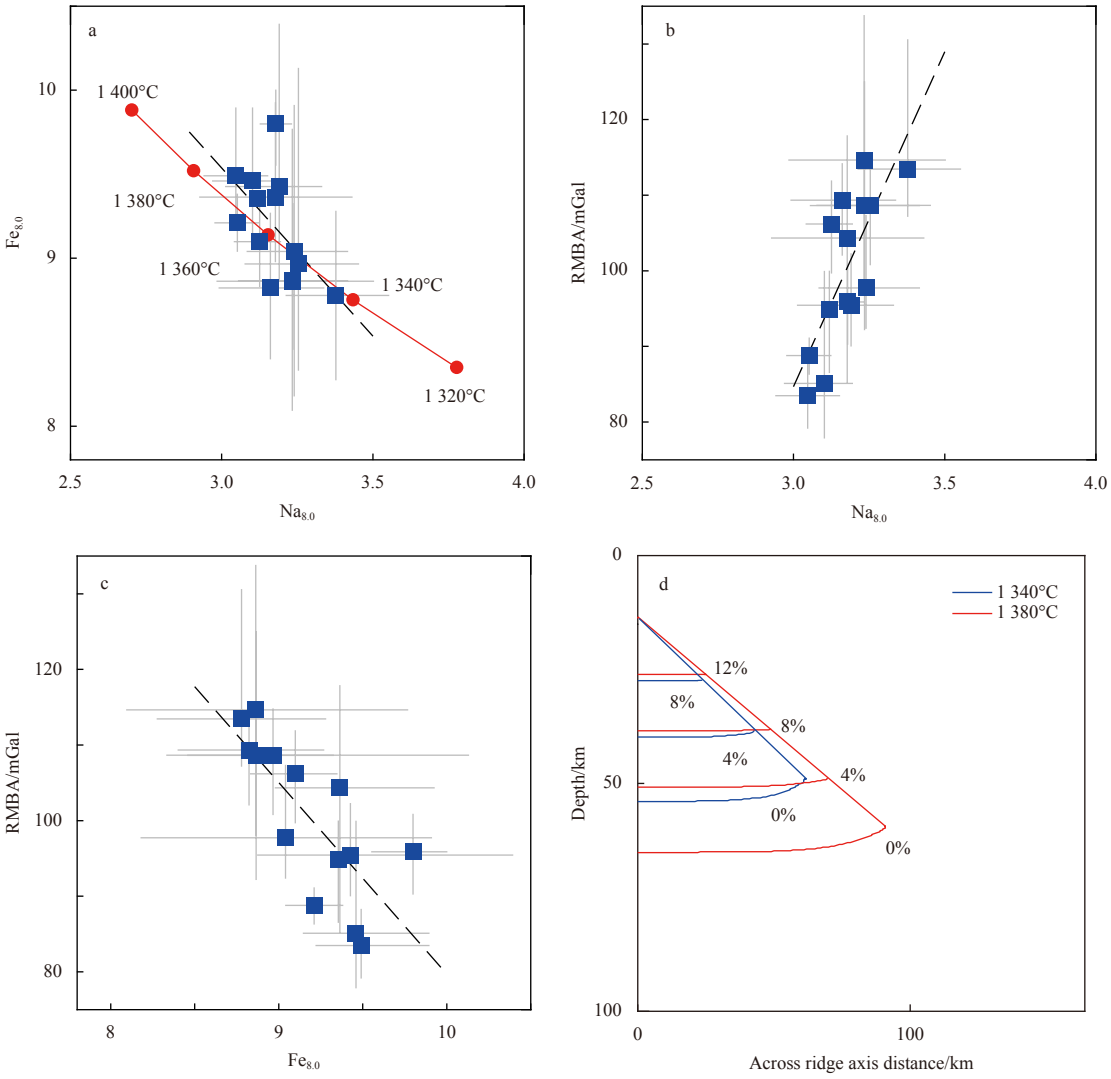


**Fig. 9.** Correlations between the averaged values of the along-axis $Na_{8.0}$ and $Fe_{8.0}$ (a), $Na_{8.0}$ and RMBA (b), and $Fe_{8.0}$ and RMBA (c); and calculated partial melting zones for mantle potential temperatures of 1 340°C (blue) and 1 380°C (red) (d). Blue squares and gray crosses in a, b and c show the averaged values and limits of intra-segment variations of each parameters, respectively. Dashed black lines show the best linear fitting. Red dots in a are the calculated values of $Na_{8.0}$ and $Fe_{8.0}$ for different mantle potential temperatures. Labels marked as percentages in d indicate the degree of melting.

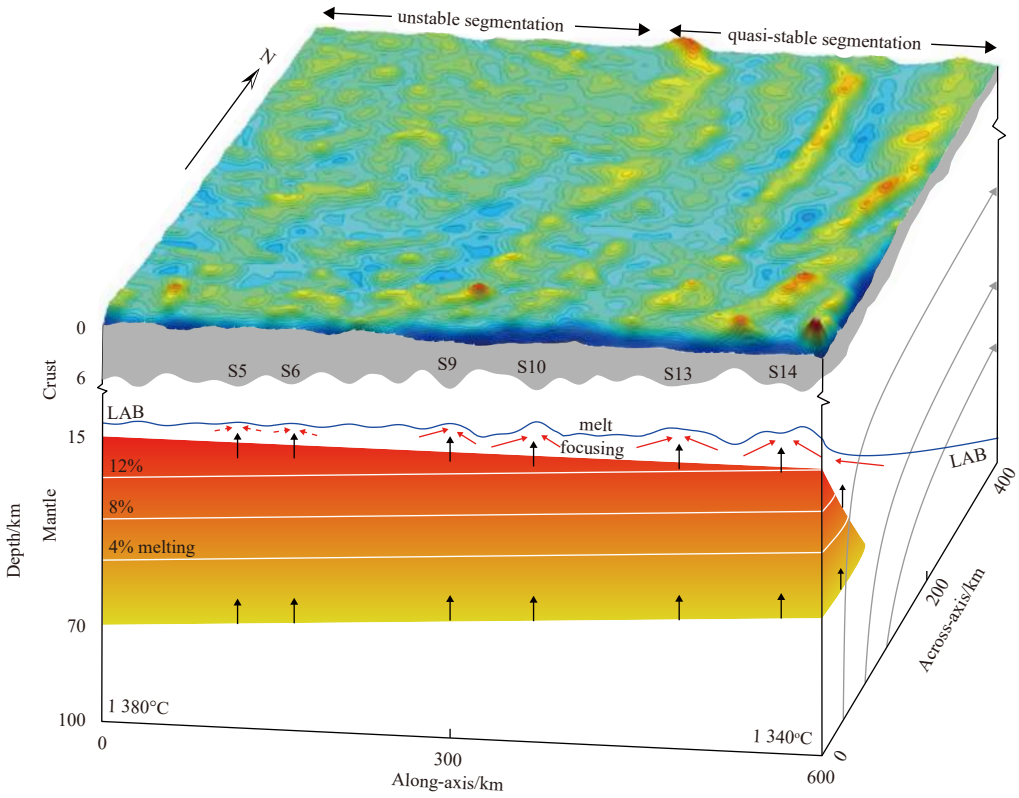


**Fig. 10.** A synthesized model showing key features of the investigated orthogonal supersegment. Top view: Residual FAA as in Fig. 1. Sections of relatively stable (eastern) and unstable (western) segmentation are shown. Front view: Along-ridge variation in crustal thickness (grey), the calculated mantle melting zone (color), and the calculated degree of partial melting (white lines). Also shown are hypothesized lithosphere-asthenosphere boundary (LAB, blue curve). Along-axis melt focusing is interpreted to be stronger at segments S9, S10, S13, and S14 (red solid arrows) than other segments (e.g., segments S5 and S6, red dashed arrows). The western region was hypothesized to have higher mantle temperature and smaller ridge-axis offset, leading to smoother LAB, less sustained magma focusing, and less stable segmentation. In contrast, the relatively large ridge-axis offsets of the eastern section may have resulted in more sustained along-axis focusing of magma supply at individual ridge segments, enabling relatively stable segmentation.

supersegment appears to correlate with the degree of along-axis melt focusing of the segments (Fig. 10). The results show that segments S9, S10, S13, and S14, which have the greatest degree of along-axis melt focusing, are also associated with relatively coherent off-axis NTD traces and thus show quasi-stable segmentation (top view, Fig. 10). In contrast, the ridge segments of the western section are associated with lower degree of along-axis melt focusing and lesser coherent off-axis NTD traces. A more complete quantification of the relationship between melt focusing and segment stability, however, requires future further investigations.

## 5 Conclusions

Analyses of gravity, magnetic, and multibeam bathymetric data of the SWIR at 16°–25°E reveal systematic along- and across-axis variations in crustal structure, reflecting significant changes in mantle temperature and melting.

(1) The results indicate that the regionally averaged crustal thickness reduced systematically from approximately 7 Ma to the present, indicating a general decrease in regional magma supply.

(2) The crustal structure is asymmetric between the conjugate ridge flanks on a regional scale. The faster-spreading southern flank is associated with a slightly thinner crust, possibly reflecting a greater degree of tectonic extension to accommodate more plate separation. However, the crustal accretion process in local scales shows strong temporal and spatial variations.

(3) The axial crustal thickness decreases systematically eastward, correlating with decreases in the average degree and initial depth of mantle melting as inferred from the observed variations in $Na_{8.0}$ and $Fe_{8.0}$. The 2D models of mantle melting suggest that the observed variations in crustal thickness and major element geochemistry can be explained by an eastward decrease in the mantle potential temperature of about 40°C from approximately 1 380°C at the western end to approximately 1 340°C at the eastern end.

(4) Segmentation in the western section of the supersegment is relatively unstable, while that of the eastern section is quasi-stable. It was hypothesized that the relatively large ridge-axis offsets in the eastern section may have resulted in sustained focusing of magma supply at the centers of individual segments and relatively stable segmentation.

***Acknowledgements***

We thank two anonymous reviewers for comments that helped to improve the manuscript. We benefited from discussion with the Deep Ocean Geodynamics Group at the South China Sea Institute of Oceanology. Figures were drawn using the GMT software of Wessel and Smith (1998).

**References**


Behn M D, Grove T L. 2015. Melting systematics in mid-ocean ridge basalts: application of a plagioclase-spinel melting model to global variations in major element chemistry and crustal thickness. Journal of Geophysical Research: Solid Earth, 120(7): 4863–4886, doi: 10.1002/2015JB011885

Bernard A, Munschy M, Rotstein Y, et al. 2005. Refined spreading history at the Southwest Indian Ridge for the last 96 Ma, with the aid of satellite gravity data. Geophysical Journal International, 162(3): 765–778, doi: 10.1111/j.1365-246X.2005.02672.x

Canales J P, Detrick R S, Lin Jian, et al. 2000. Crustal and upper mantle seismic structure beneath the rift mountains and across a nontransform offset at the Mid-Atlantic Ridge (35°N). Journal of Geophysical Research: Solid Earth, 105(B2): 2699–2719, doi: 10.1029/1999JB900379

Cannat M, Rommevaux-Jestin C, Fujimoto H. 2003. Melt supply variations to a magma-poor ultra-slow spreading ridge (Southwest Indian Ridge 61° to 69°E). Geochemistry, Geophysics, Geosystems, 4(8): 9104, doi: 10.1029/2002GC000480

Carbotte S M, Smith D K, Cannat M, et al. 2015. Tectonic and magmatic segmentation of the Global Ocean Ridge System: a synthesis of observations. Geological Society of London, 420(1): 249–295, doi: 10.1144/SP420.5

Dalton C A, Langmuir C H, Gale A. 2014. Geophysical and geochemical evidence for deep temperature variations beneath mid-ocean ridges. Science, 344(6179): 80–83, doi: 10.1126/science.1249466

Dannowski A, Phipps Morgan J, Grevemeyer I, et al. 2018. Enhanced mantle upwelling/melting caused segment propagation, oceanic core complex die off, and the death of a transform fault: the Mid-Atlantic Ridge at 21.5°N. Journal of Geophysical Research: Solid Earth, 123(2): 941–956, doi: 10.1002/2017JB014273

DeMets C, Merkouriev S, Sauter D. 2015. High-resolution estimates of Southwest Indian Ridge plate motions, 20 Ma to present. Geophysical Journal International, 203(3): 1495–1527, doi: 10.1093/gji/ggv366

Dick H J B, Lin Jian, Schouten H. 2003. An ultraslow-spreading class of ocean ridge. Nature, 426(6965): 405–412, doi: 10.1038/nature02128

Escartín J, Cowie P A, Searle R C, et al. 1999. Quantifying tectonic strain and magmatic accretion at a slow spreading ridge segment, Mid-Atlantic Ridge, 29°N. Journal of Geophysical Research: Solid Earth, 104(B5): 10421–10437, doi: 10.1029/1998JB900097

Forsyth D W. 1993. Crustal thickness and the average depth and degree of melting in fractional melting models of passive flow beneath mid-ocean ridges. Journal of Geophysical Research: Solid Earth, 98(B9): 16073–16079, doi: 10.1029/93JB01722

Fox P J, Gallo D G. 1984. A tectonic model for ridge-transform-ridge plate boundaries: implications for the structure of oceanic lithosphere. Tectonophysics, 104(3–4): 205–242

Gente P, Pockalny R A, Durand C, et al. 1995. Characteristics and evolution of the segmentation of the Mid-Atlantic Ridge between 20°N and 24°N during the last 10 million years. Earth and Planetary Science Letters, 129(1–4): 55–71

Georgen J E, Lin Jian, Dick H J B. 2001. Evidence from gravity anomalies for interactions of the Marion and Bouvet hotspots with the Southwest Indian Ridge: effects of transform offsets. Earth and Planetary Science Letters, 187(3–4): 283–300

Gregg P M, Behn M D, Lin Jian, et al. 2009. Melt generation, crystallization, and extraction beneath segmented oceanic transform faults. Journal of Geophysical Research: Solid Earth, 114(B11): B11102

Grindlay N R, Madsen J A, Rommevaux-Jestin C, et al. 1998. A different pattern of ridge segmentation and mantle Bouguer gravity anomalies along the ultra-slow spreading Southwest Indian Ridge (15°30'E to 25°E). Earth and Planetary Science Letters, 161(1–4): 243–253

Hooft E E E, Detrick R S, Toomey D R, et al. 2000. Crustal thickness and structure along three contrasting spreading segments of the Mid-Atlantic Ridge, 33.5°–35°N. Journal of Geophysical Research: Solid Earth, 105(B4): 8205–8226, doi: 10.1029/1999JB900442

Hosford A, Lin Jian, Detrick R S. 2001. Crustal evolution over the last 2 m.y. at the Mid-Atlantic Ridge OH-1 segment, 35°N. Journal of Geophysical Research, 106(B7): 13269–13285, doi: 10.1029/2001JB000235

Kuo B Y, Forsyth D W. 1988. Gravity anomalies of the ridge-transform system in the South Atlantic between 31° and 34.5°S: upwelling centers and variations in crustal thickness. Marine Geophysical Researches, 10(3–4): 205–232

Lin Jian, Phipps Morgan J. 1992. The spreading rate dependence of three-dimensional mid-ocean ridge gravity structure. Geophysical Research Letters, 19(1): 13–16, doi: 10.1029/91GL03041

Lin Jian, Purdy G, Schouten H, et al. 1990. Evidence from gravity data for focusedmagmatic accretionalong the Mid-Atlantic Ridge. Nature, 344(6267): 627–632, doi: 10.1038/344627a0

Macdonald K C, Scheirer D S, Carbotte S M. 1991. Mid-ocean ridges: discontinuities, segments and giant cracks. Science, 253(5023): 986–994, doi: 10.1126/science.253.5023.986

Magde L S, Sparks D W. 1997. Three-dimensional mantle upwelling, melt generation, and melt migration beneath segment slow spreading ridges. Journal of Geophysical Research: Solid Earth, 1997(B9): 20571–20583

Müller R D, Sdrolias M, Gaina C, et al. 2008. Age, spreading rates, and spreading asymmetry of the world's ocean crust. Geochemistry, Geophysics, Geosystems, 9(4): Q04006, doi: 10.1029/2007GC001743

Pariso J E, Sempéré J C, Rommevaux C. 1995. Temporal and spatial variations in crustal accretion along the Mid-Atlantic Ridge (29°–31°30′N) over the last 10 m.y.: implications from a three-dimensional gravity study. Journal of Geophysical Research: Solid Earth, 100(B9): 17781–17794, doi: 10.1029/95JB01146

Parker R L. 1973. The rapid calculation of potential anomalies. Geophysical Journal International, 31(4): 447–455, doi: 10.1111/j.1365-246X.1973.tb06513.x

Patriat P, Sauter D, Munschy M, et al. 1997. A survey of the Southwest Indian Ridge axis between Atlantis II fracture zone and the Indian Ocean triple junction: regional setting and large scale segmentation. Marine Geophysical Researches, 19(6): 457–480, doi: 10.1023/A:1004312623534

Phipps Morgan J, Forsyth D W. 1988. Three-dimensional flow and temperature perturbations due to a transform offset: effects on oceanic crustal and upper mantle structure. Journal of Geophysical Research: Solid Earth, 93(B4): 2955–2966, doi: 10.1029/JB093iB04p02955

Sandwell D T, Müller R D, Smith W H F, et al. 2014. New global marine gravity model from CryoSat-2 and Jason-1 reveals buried tectonic structure. Science, 346(6205): 65–67, doi: 10.1126/science.1258213

Sauter D, Patriat P, Rommevaux-Jestin C, et al. 2001. The Southwest Indian Ridge between 49°15′E and 57°E: focused accretion and magma redistribution. Earth and Planetary Science Letters, 192(3): 303–317, doi: 10.1016/S0012-821X(01)00455-1

Schouten H, Klitgord K D, Whitehead J A. 1985. Segmentation of mid-ocean ridges. Nature, 317(6034): 225–229, doi: 10.1038/317225a0

Sempéré J C, Lin Jian, Brown H S, et al. 1993. Segmentation and morphotectonic variations along a slow-spreading center: the Mid-Atlantic Ridge (24°00′N–30°40′N). Marine Geophysical Researches, 15(3): 153–200, doi: 10.1007/BF01204232

Sparks D W, Parmentier E M, Phipps Morgan J. 1993. Three-dimensional mantle convection beneath a segmented spreading center: implications for along-axis variations in crustal thickness and gravity. Journal of Geophysical Research: Solid Earth, 98(B12): 21977–21995, doi: 10.1029/93JB02397

Standish J J, Dick H J B, Michael P J, et al. 2008. MORB generation beneath the ultraslow spreading Southwest Indian Ridge (9°–25°E): major element chemistry and the importance of process versus source. Geochemistry, Geophysics, Geosystems, 9(5): Q05004, doi: 10.1029/2008GC001959

Tolstoy M, Harding A J, Orcutt J A. 1993. Crustal thickness on the Mid-Atlantic Ridge: bull's-eye gravity anomalies and focused accretion. Science, 262(5134): 726–729, doi: 10.1126/science.262.5134.726

Tozer B, Sandwell D T, Smith W H F, et al. 2019. Global bathymetry and topography at 15 arc sec: SRTM15+. Earth and Space Sci-

ence, 6: 1847–1864, doi: 10.1029/2019EA000658
Tucholke B E, Lin Jian, Kleinrock M C, et al. 1997. Segmentation and crustal structure of the western Mid-Atlantic Ridge flank, 25°25′–27°10′N and 0–29 m.y. Journal of Geophysical Research: Solid Earth, 102(B5): 10203–10223, doi: 10.1029/96JB03896
Wang T T, Tucholke B E, Lin Jian. 2015. Spatial and temporal variations in crustal production at the Mid-Atlantic Ridge, 25°N–27°30′N and 0–27 Ma. Journal of Geophysical Research: Solid Earth, 120(4): 2119–2142, doi: 10.1002/2014JB011501
Wessel P, Smith W H F. 1998. New, improved version of generic mapping tools released. Eos, Transactions American Geophysical Union, 79(47): 579, doi: 10.1029/98EO00426
Yang H J, Kinzler R J, Grove T L, et al. 1996. Experiments and models of anhydrous, basaltic olivine-plagioclase-augite saturated melts from 0.001 to 10 kbar. Contributions to Mineralogy and Petrology, 124(1): 1–18, doi: 10.1007/s004100050169
Zhang Fan, Lin Jian, Zhang Xubo, et al. 2018. Asymmetry in oceanic crustal structure of the South China Sea basin and its implications on mantle geodynamics. International Geology Review, 62(7–8): 840–858, doi: 10.1080/00206814.2018.1425922
Zhang Tao, Lin Jin, Gao Jinyao. 2019. Asymmetric crustal structure of the ultraslow-spreading Mohns Ridge. International Geology Review, 62(5): 568–584, doi: 10.1080/00206814.2019.1627586
Zheng Tingting, Tucholke B E, Lin Jian. 2019. Long-term evolution of nontransform discontinuities at the Mid-Atlantic Ridge, 24°N–27°30′N. Journal of Geophysical Research: Solid Earth, 124(10): 10023–10055, doi: 10.1029/2019JB017648

## Supplementary information:

**Fig. S1.** Method of calculating residual free-air anomaly (RFAA). Gray dots are original FAA data points, the yellow line shows the age dependence of the FAA averaged in bins of 0.5 Ma, and the red line is the best-fitting square root decrease in the FAA for crustal age greater than 3 Ma.

**Fig. S2.** Mean and standard deviations of spreading rates of the southern (red) and northern flanks (blue) of the entire study area. The arrows and letters indicate the magnetic anomaly reversals used in calculating spreading rates.

**Fig. S3.** Calculated gravity correction based on the 3D models of passive mantle upwelling driven by asymmetric seafloor spreading. The red line indicates the simplified plate boundary. Du Toit TF: Du Toit transform fault; SWIR: Southwest Indian Ridge.

The supplementary information is available online at https://doi.org/10.1007/s13131-021-1724-3 and www.aosocean.com. The supplementary information is published as submitted, without typesetting or editing. The responsibility for scientific accuracy and content remains entirely with the authors.